
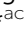



















PAPER

[View Article Online](#)
[View Journal](#) | [View Issue](#)Cite this: *J. Mater. Chem. B*,
2024, 12, 10915Assembly-enhanced indocyanine green
nanoparticles for fluorescence imaging-guided
photothermal therapy†Shukun Li,^{ab} Yudong Li,^b Mengqian Shi,^a Ruirui Xing,^{*ac} Jan C. M. Van Hest^b
and Xuehai Yan^b                   

The development of theranostic agents that offer complete biocompatibility, coupled with enhanced diagnostic and therapeutic performance, is crucial for fluorescence imaging-guided photothermal therapy in anti-tumor applications. However, the fabrication of nanotheranostics meeting the aforementioned requirements is challenged by concerns regarding biosafety and limited control over construction. Herein, we reported a class of fluorescence imaging-guided photothermal theranostic nanomaterials that are composed of amino acid derivatives and clinically used small photoactive indocyanine green molecules. Through manipulation of noncovalent interactions, these binary building blocks can co-assemble into nanoparticles in a tunable manner. Significantly, such construction not only maintained the fluorescence properties of photoactive molecules, but also enhanced their stability to overcome barriers from photodegradation and complex physiological conditions. These collective features integrated their precise anti-tumor applications, including fluorescence imaging diagnosis and photothermal ablation therapy. This study reported a class of nanotheranostics characterized by biocompatibility, adjustable construction, and robust stability, which are beneficial for the clinical translation of fluorescence imaging-guided photothermal therapy against tumors.

Received 23rd July 2024,
Accepted 18th September 2024

DOI: 10.1039/d4tb01604a

rsc.li/materials-b

Introduction

Photothermal therapy (PTT) is a noninvasive and localized therapeutic modality for cancer treatment, which can convert light energy absorbed by photothermal agents into heat, rising the local temperature as to rapidly kill the tumor entity.^{1–5} Furthermore, imaging-guided PTT, which is assisted by diagnostic techniques to indicate the biodistribution of photothermal agents in a real-time manner, enables a more precise anti-cancer outcome.^{6–9} With the continuous development of nanotechnology, theranostic materials for imaging-guided PTT have been widely fabricated.^{10–13} These nanomaterials aim to tailor therapeutic performance but still face challenges when considering their potential clinical theranostic applications. Specifically, many theranostic agents with dual imaging and

therapeutic functions are composed of nonbiodegradable components, such as nanocarbons¹⁴ and noble metal quantum dots,¹⁵ whose biological applications are inhibited by their long-term toxicity.¹⁶ By contrast, biocompatible organic nanomaterials, which predominantly involve the entrapment of photothermal agents and fluorescent probes in one platform, such as liposomes,¹⁷ micelles¹⁸ and polymeric nanostructures,¹⁹ have addressed the shortcomings associated with inorganic non-degradability.²⁰ Unfortunately, the integration of multiple components is hindered by challenges such as controllability, low entrapment efficiency, and insufficient stability.²¹ Therefore, there is still a need to develop completely biocompatible nanotheranostic materials, particularly for utilizing biosafe biomolecules and simultaneously improving the theranostic performance.

Indocyanine green (ICG) is a near-infrared cyanine dye and has been approved by the U.S. Food and Drug Administration (FDA) as a fluorescent contrast agent for medical diagnosis.²² Moreover, numerous studies have demonstrated its photothermal utility due to its strong absorption and deep penetration.^{23–26} However, despite the combined fluorescent and photothermal properties, the anti-tumor applications of ICG are extremely hindered by its photodegradation instability.²⁷ The utilization of peptide co-assembly, employing a spontaneous strategy based

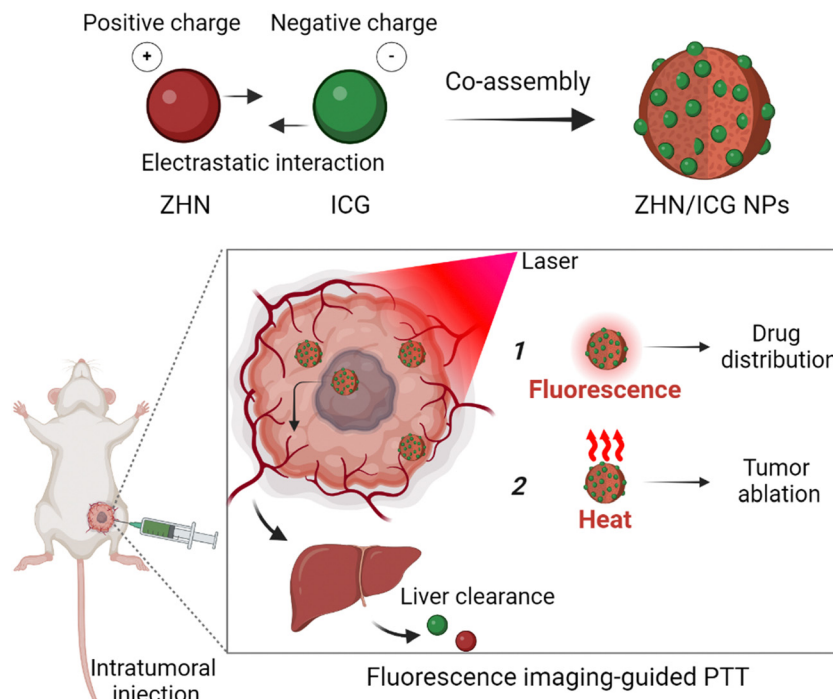
^a State Key Laboratory of Biochemical Engineering, Key Laboratory of Biopharmaceutical Preparation and Delivery, Institute of Process Engineering, Beijing 100190, China. E-mail: rrxing@ipe.ac.cn, yanxh@ipe.ac.cn

^b Bio-Organic Chemistry, Institute for Complex Molecular Systems, Eindhoven University of Technology, P.O. Box 513, 5600 MB Eindhoven, The Netherlands

^c School of Chemical Engineering, University of Chinese Academy of Sciences, Beijing 100049, China

† Electronic supplementary information (ESI) available. See DOI: <https://doi.org/10.1039/d4tb01604a>





Scheme 1 Schematic illustration of fabrication of nanoparticles and their fluorescence imaging-guided photothermal therapy.

on noncovalent interactions to efficiently disperse molecules within nanostructures, could provide protection for ICG and therefore overcome the aforementioned issues.^{28–31} In this regard, we present the peptide–ICG co-assemblies for fluorescence imaging-guided PTT (Scheme 1). Short peptides, even amino acid derivatives, are promising candidates for engineering nanomaterials owing to their natural occurrence and tunable noncovalent interactions.^{32–34} Therefore, a histidine derivative (Z-His-NH₂, ZHN) was selected as a modulating molecule to control co-assembly with the ICG molecule. By manipulating electrostatic interactions and other noncovalent interactions between ICG and ZHN, we achieved the fluorescent and photothermal nanoparticles (NPs) with high entrapment efficiency of ICG (up to 94.5% calculated). Importantly, these nanoparticles not only maintained the intrinsic fluorescence emission of ICG, but also significantly improved the stability of photothermal conversion and resistance to complex physiological conditions. Taken together, these properties of ZHN/ICG NPs made them suitable for localized tumor injection with a reliable drug dosage, thereby realizing spontaneous fluorescence imaging and photothermal ablation. This work reported a kind of fluorescence imaging-guided photothermal nanotheranostics characterized by biocompatibility, controllable construction, and considerable stability, highlighting their potential clinical translation in anti-tumor applications.

Results and discussion

Characterization of ZHN/ICG NPs

The histidine derivative, Z-His-NH₂ (ZHN) (Fig. S1, Electronic supplementary information, ESI†), because of its positively

charged nature, has been selected as the building block for co-assembling with negatively charged indocyanine green (ICG) (Fig. S2, ESI†). Driven by the electrostatic interaction, combining with other interactions, such as the hydrogen bonds linked by the sulfonate groups of ICG and amide groups of ZHN³⁵ and hydrophobic association occurred within aromatic groups of these binary building blocks,³⁶ they co-assembled into ZHN/ICG nanostructures. As shown in Fig. S3 (ESI†) and Table S1 (ESI†), the size of these nanostructures increased with rising ICG concentration, which can be explained that more negatively charged ICG molecules interacted with more positively charged ZHN molecules (isoelectric point 7.59) at a pH value of 6.5, resulting in the formation of larger structures. It is of significance to verify the electrostatic interaction, hence, we further changed the pH value of co-assembly systems. Fig. S4a (ESI†) and Table S2 (ESI†) show that the nanostructures formed at pH 3.3 were comparatively smaller than those at pH 6.5. This can be attributed to the protonation of imidazole groups below the isoelectric point,³⁷ which imparts more positive charge to ZHN molecules, enhancing co-assembly with ICG. Additionally, the zeta potential of the nanostructures at pH 3.3 was more negative compared to that at pH 6.5 (Fig. S4b, ESI†), indicating that more negatively charged ICG molecules are attracted by ZHN molecules. These findings confirm the role of electrostatic attraction in the formation of the nanostructures. Moreover, another histidine derivative, Z-His-NHNH₂ (ZHNN) (Fig. S5, ESI†), possessing a similar structure to ZHN, could also co-assemble with ICG. Not surprisingly, the nanostructures can also be tuned (Fig. S6 and Table S3, ESI†), indicating the universality of this facile strategy.

Since the entrapment efficiency is critical for nanotheranostics design,³⁸ we systematically measured it by varying the



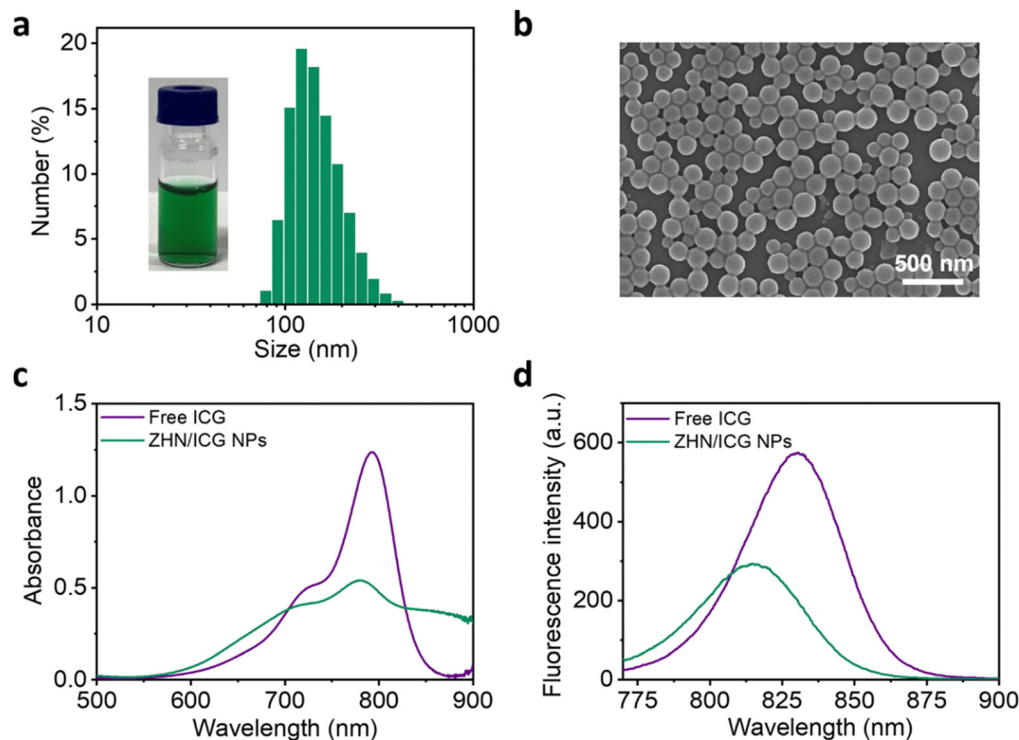


Fig. 1 Characterization of ZHN/ICG NPs. (a) The DLS measurement of ZHN/ICG NPs. The inset shows their optical picture. (b) The SEM image of ZHN/ICG NPs. Comparison of the (c) absorbance spectra and (d) fluorescence spectra of free ICG and ZHN/ICG NPs.

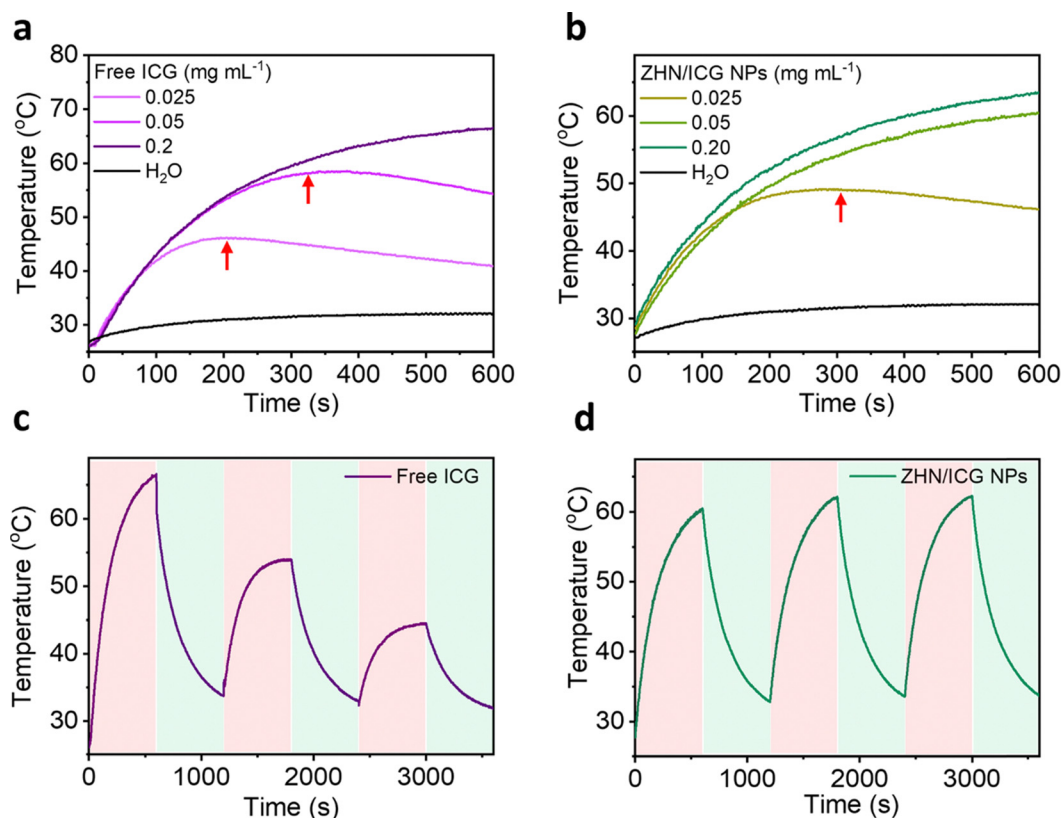


Fig. 2 Photothermal performance of ZHN/ICG NPs. The concentration-dependent temperature elevation of (a) free ICG and (b) ZHN/ICG NPs under 808 nm laser irradiation (2 W cm^{-2} , 10 min). The red arrows indicate the onset degradation time. Three heating-cooling cycles of (c) free ICG and (d) ZHN/ICG NPs at an ICG concentration of 0.2 mg mL^{-1} under 808 nm laser irradiation.



ZHN:ICG mass ratio. In Fig. S7 (ESI[†]), the entrapment efficiencies of ZHN and ICG in nanostructures fabricated with a ZHN:ICG mass ratio of 5:1 were found to be 63.5% and 94.5%, respectively. This performance is superior to that observed with other mass ratios such as 20:1, 10:1, and 3.3:1. The optimal ratio of 5:1 provided an adequate balance between ZHN and ICG, leading to enhanced encapsulation efficiency of ICG molecules. Deviations from this optimal ratio resulted in less efficient encapsulation. For instance, at a ZHN:ICG mass ratio of 20:1, the excess ZHN molecules do not effectively stabilize a high amount of ICG, leading to lower encapsulation efficiency. Conversely, at a ratio of 3.3:1, the insufficient amount of ZHN may result in excessive ICG molecules that are not adequately encapsulated, also reducing overall efficiency. Therefore, the ZHN:ICG mass ratio of 5:1 was selected for subsequent experiments due to its optimal performance in entrapment efficiency of ICG molecules. At this mass ratio, the obtained ZHN/ICG nanoparticles (NPs) possessed a uniform hydraulic diameter of 153.0 ± 52.3 nm and a ζ potential of -37.3 mV, as characterized by dynamic light scattering (DLS) results (Fig. 1a and Fig. S8, ESI[†]). The relatively high surface charge of the ZHN/ICG NPs, due to electrostatic repulsion, contributed to their stable dispersion in solution, preventing aggregation. Morphological characterization including scanning electron microscopy (SEM) (Fig. 1b) and transmission electron microscopy (TEM) images (Fig. S9, ESI[†]) demonstrated that ZHN/ICG NPs were in a regular spherical shape, in which the

size was in line with the DLS result. Furthermore, the absorption band of ICG molecules in ZHN/ICG NPs showed a decrease while broadened to the wavelength up to 900 nm (Fig. 1c), possibly because of the electron delocalization of ICG molecules promoted by their noncovalent interactions with ZHN,²⁹ suggesting a co-assembly process. Of note, the obtained ZHN/ICG NPs were still fluorescent (Fig. 1d), differing in the quenching effect of chromophores caused by aggregation,¹ which is possibly because the shortened intermolecular distances restrict the alkene motion of ICG molecules and thereby endow them with excellent dispersibility in ZHN/ICG NPs,^{35,39} rather than their self-aggregation. These results demonstrate the fluorescence imaging potential of ZHN/ICG NPs.

Photothermal performance of ZHN/ICG NPs

As far, we have demonstrated the fluorescence properties of ZHN/ICG NPs, and then we investigated their photothermal performance. ICG molecules are easily degraded upon photo-irradiation due to the saturation of the double bonds in their conjugated chains,⁴⁰ rendering the poor stability of photothermal conversion. When ICG molecules co-assembled with ZHN, they exhibited distinct behaviors. As depicted in Fig. 2a and b, free ICG and ZHN/ICG NPs with the same high concentration of 0.2 mg mL^{-1} , both showed considerable photostability at a laser power density of 2 W cm^{-2} , owing to that the sufficient molecules can realize efficient photothermal conversion within 10 min. The maximum temperature within 10 min of free ICG

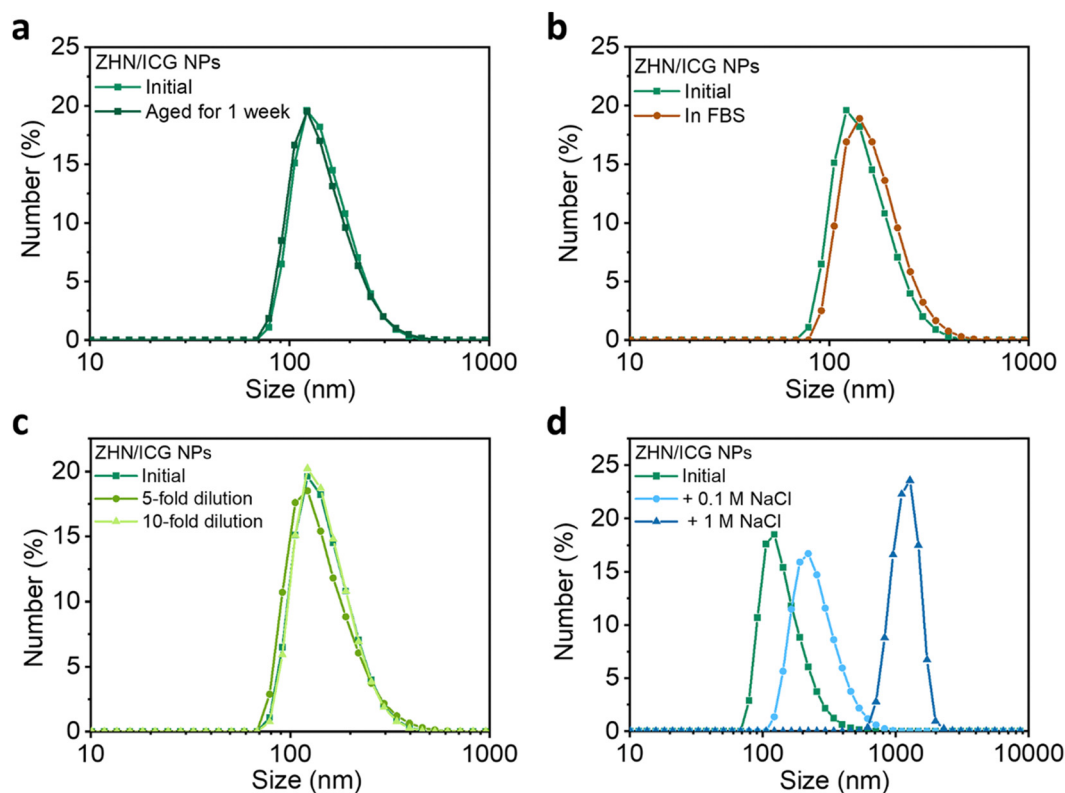


Fig. 3 Stability test of ZHN/ICG NPs. DLS profiles of (a) freshly prepared and aged ZHN/ICG NPs, (b) ZHN/ICG NPs dispersed in FBS, (c) ZHN/ICG NPs with various dilutions, and (d) ZHN/ICG NPs dispersed under different NaCl conditions.



and ZHN/ICG NPs reached 66.4 °C and 63.5 °C, respectively. However, when reducing the ICG concentration to 0.025 mg mL⁻¹, differences between free ICG and ZHN/ICG NPs appeared. The temperature of ZHN/ICG NPs could continuously rise, while the free ICG started to degrade at 324 s. Intriguingly, at a concentration of 0.025 mg mL⁻¹, although both of them showed degradation, the onset degradation time of free ICG was 205 s, while that of the corresponding counterpart of ZHN/ICG NPs was 303 s. However, the control group of pure water exhibited a negligible temperature increase. These results demonstrated the improved photothermal conversion stability of ZHN/ICG NPs. Interestingly, the photothermal conversion efficiency (η) was calculated using a reported method,⁴¹ yielding 39.83% for ZHN/ICG NPs and 29.0% for free ICG. Also, the photothermal conversion of ZHN/ICG NPs was conducted by 808 nm laser heating for 10 min and followed by natural cooling at room temperature for another 10 min. As shown in Fig. 2c, during three cycles of photoirradiation, free ICG only tolerated one cycle of laser irradiation. By contrast, ZHN/ICG NPs maintained a high photothermal effect (Fig. 2d), confirming their enhanced capability of photothermal conversion. By these comparisons, the improved photostability of ICG molecules could be ascribed to the well-defined nanostructures. That is, ICG molecules were

trapped and dispersed within ZHN/ICG NPs after co-assembly with ZHN, which not only limited their self-aggregation to impair fluorescence, but also significantly isolated their conjugated chains from oxidation, and thus avoided further degradation. Given the fluorescence properties revealed above and the robust photothermal effect, the ZHN/ICG NPs are expected to become promising nanotheranostics for imaging-guided photothermal therapy.

Stability test of ZHN/ICG NPs

The stability of nanomaterials is the prerequisite for biomedical applications.^{42,43} To this end, a series of stability tests were conducted (Fig. 3 and Table S4, ESI†). The ZHN/ICG NPs showed a negligible change in terms of size over time (Fig. 3a), which indicates that ZHN/ICG NPs had suitable stability for long term storage. The stability of ZHN/ICG NPs in the fetal bovine serum (FBS) medium that mimicked a cell culture environment was further monitored.⁴⁴ When incubating ICG NPs in 10% FBS solution (v/v) at 37 °C for 24 h, the size and distribution of ZHN/ICG NPs remained stable as shown in Fig. 3b, and a slight increase in size was owing to the slight hydrophobic interactions between FBS and ZHN/ICG NPs. In addition, the size distribution was also kept well by various

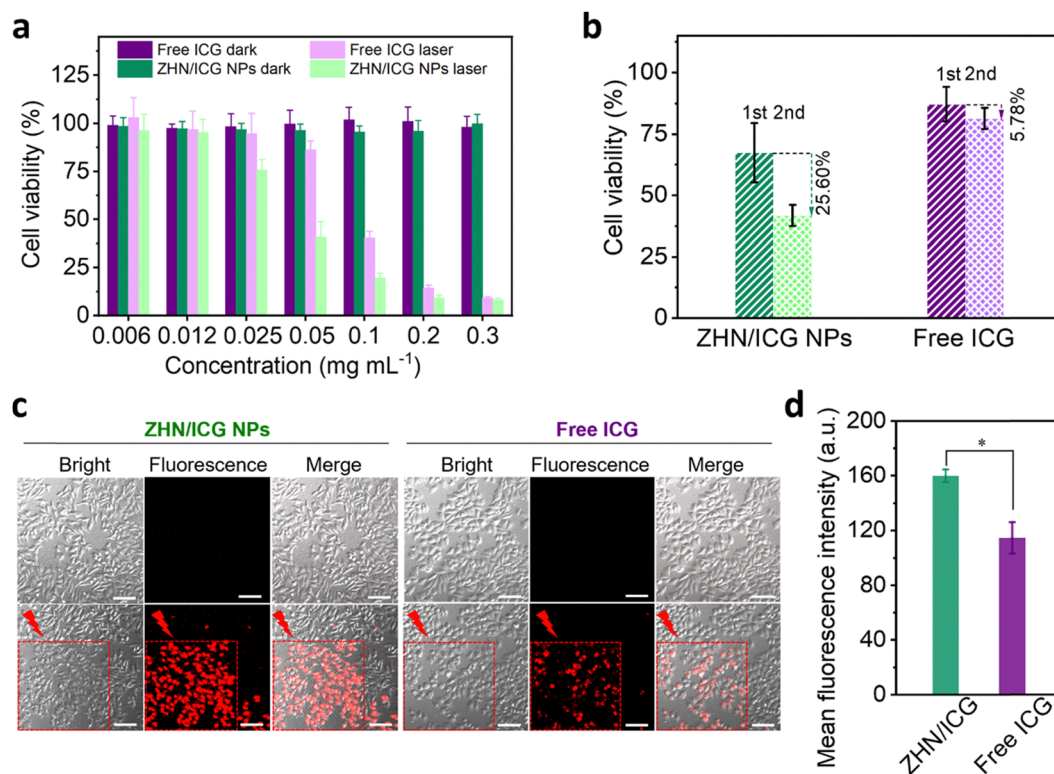


Fig. 4 *In vitro* evaluation of ZHN/ICG NPs. (a) The MTT assay of MCF-7 cells after exposure to different concentrations of ZHN/ICG NPs and free ICG (ICG concentration: 0.006–0.3 mg mL⁻¹) with or without 808 nm laser irradiation (1.5 W cm⁻², 1 min). Error bars represent the standard deviation ($n = 6$). (b) Cell viability of MCF-7 cells after incubation with the ZHN/ICG NPs and free ICG (ICG concentration 0.025 mg mL⁻¹) and irradiated twice using an 808 nm laser (1.5 W cm⁻², 1 min). Error bars represent the standard deviation ($n = 6$). (c) CLSM images of MCF-7 cells stained with the PI dye. Before staining, MCF-7 cells were respectively incubated with ZHN/ICG NPs and free ICG (ICG concentration 0.15 mg mL⁻¹) for 24 h, followed by 808 nm laser irradiation (1.5 W cm⁻², 1 min). (d) Quantitative analysis of the mean fluorescence intensity of MCF-7 cells after the treatment from Fig. (c). Error bars represent the standard deviation ($n = 3$), and P values are calculated by one-way ANOVA * $P < 0.05$.



folds of dilution (Fig. 3c). Furthermore, NaCl was added to the initial ZHN/ICG NP solution (Fig. 3d). The higher the concentration of NaCl, the larger the size of ZHN/ICG NPs. This phenomenon can be interpreted as the charge shielding effect of NaCl that induced the aggregation of ZHN/ICG NPs, which led us to conclude that electrostatic repulsion contributed to the dispersion of ZHN/ICG NPs, enabling the stability in aqueous solution. These results demonstrate the superior stability of ZHN/ICG NPs, thus paving the way for their *in vitro* and *in vivo* applications.

In vitro evaluation of ZHN/ICG NPs

Next, the photothermal conversion of ZHN/ICG NPs was investigated *in vitro*. Drug formulations including free ICG and ZHN/ICG NPs with a series of concentrations were respectively incubated with human breast adenocarcinoma cancer (MCF-7) cells (Fig. 4a). After incubation for 24 h, no discernible cytotoxicity was observed under dark conditions, even at a high concentration of 0.3 mg mL^{-1} , confirming the high biocompatibility of ICG molecules and ZHN/ICG NPs. By contrast, through 808 nm laser irradiation (1.5 W cm^{-2} , 1 min), the viability of cells showed a concentration-dependent decrease. The IC_{50} value of ZHN/ICG NPs was $43.16 \text{ } \mu\text{g mL}^{-1}$, which is almost

twice lower than $82.65 \text{ } \mu\text{g mL}^{-1}$ of free ICG. The result may be due to the improved stability of ZHN/ICG NPs that enabled them to be well dispersed in cell culture media and achieved robust photothermal conversion within cells.⁴⁵ Furthermore, the cells that respectively incubated with ZHN/ICG NPs (ICG concentration: 0.025 mg mL^{-1}) and free ICG (ICG concentration: 0.025 mg mL^{-1}) were irradiated twice with the 808 nm laser (Fig. 4b). In the free ICG group, the cell viability after these two irradiations showed a slightly decrease of 5.78%, *i.e.*, from 87.15% to 81.37%, while the corresponding value in the ZHN/ICG NPs group decreased by 25.60%, *i.e.*, from 67.45% to 41.85%. These comparative results confirmed that the enhanced therapeutic effect of ZHN/ICG is indeed caused by their significantly improved stability. As an intuitive method to indicate the *in vitro* photothermal effect, the CLSM imaging technique was adopted. After drug formulations incubation and laser irradiation, the cells were stained by the propidium iodide (PI) dye to distinguish dead cells.⁴⁶ Apparently, in the area covered by laser irradiation, abundant red fluorescence signals were observed (Fig. 4c). Moreover, the mean fluorescence intensity of PI in the ZHN/ICG NPs group was much higher than that in the free ICG group (Fig. 4d). A detailed image (Fig. S10, ESI†) of the ZHN/ICG NP group showed the typical nucleus shrinkage after laser irradiation,

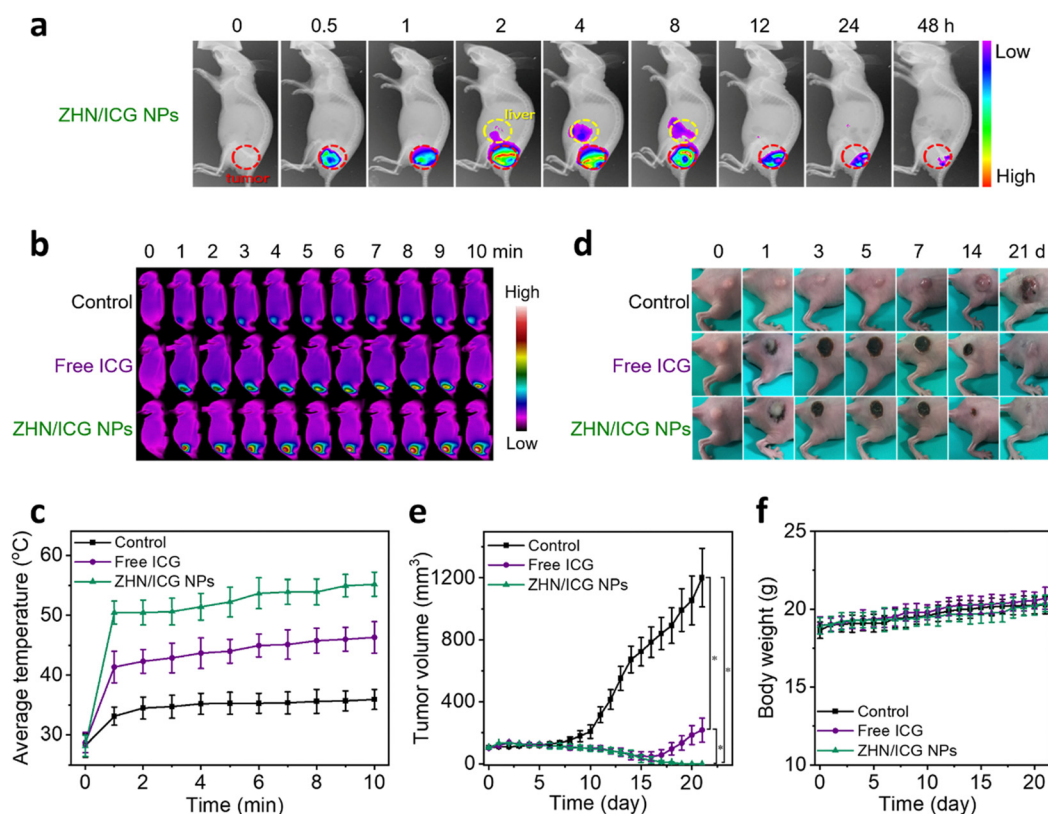


Fig. 5 *In vivo* evaluation of ZHN/ICG NPs. (a) Fluorescence images of mice bearing MCF-7 tumors after intratumorally injected with ZHN/ICG NPs (1.5 mg mL^{-1} , $50 \text{ } \mu\text{L}$) at different time intervals. The red circles indicate the tumor and the yellow circles indicate the liver. (b) Representative IR thermal images and (c) the average temperature of mice bearing MCF-7 tumors upon 808 nm laser irradiation (0.8 W cm^{-2} , 10 min) at 4 h post-injection of ZHN/ICG NPs and free ICG (ICG concentration of 1.5 mg mL^{-1} , $50 \text{ } \mu\text{L}$), respectively. Error bars represent the standard deviation ($n = 6$). (d) Representative images, (e) tumor volumes, and (f) body weights of mice bearing MCF-7 tumors at different time intervals after treatment. Error bars represent the standard deviation ($n = 6$), and P values are calculated by one-way ANOVA $*P < 0.05$.



indicating cell apoptosis. Taken together, these results suggest that the compatible ZHN/ICG NPs have significant cell-killing ability after laser excitation, highlighting the possibility for *in vivo* applications.

In vivo fluorescence imaging-guided PTT

Since the ZHN/ICG NPs retained the intrinsic fluorescence of ICG molecules, which can be used as imaging contrast to indicate the drug distribution, we first conducted the *in vivo* fluorescence imaging of ZHN/ICG NPs. The intratumoral injection mode, an emerging dosing delivery owing to its preferable drug accumulation and distribution in tumor tissue,⁴⁷ was employed. After the injection of ZHN/ICG NPs (1.5 mg mL⁻¹, 50 μL), the mice were monitored (Fig. 5a), and the average fluorescence intensity in the tumor and liver was analyzed (Fig. S11, ESI†). The fluorescence in the tumor gradually increased within 4 h after injection, demonstrating the fully dispersion of ZHN/ICG NPs. In the subsequent time intervals from 4 h to 48 h, the fluorescence in the tumor gradually weakened, while the fluorescence in the liver showed a gradual increase, especially from 2 h to 8 h, followed by a decrease after 8 h, probably owing to the quick clearance of ZHN/ICG NPs from the body through liver metabolism.⁴⁸ Taking the optimal drug distribution into consideration, 4 h post-injection was selected as the therapeutic window. The mice tumors were respectively injected with PBS (control), free ICG, and ZHN/ICG NPs and further irradiated using an 808 nm laser (0.8 W cm⁻², 10 min) under the aforementioned time window. An IR thermal mapping camera was used to monitor the real-time photothermal conversion *in situ* (Fig. 5b and c). By comparison, the average temperature of mice tumors in the ZHN/ICG NPs group was elevated to 55.2 °C at the end of irradiation, which was much higher than 46.3 °C in the free ICG group. Additionally, the average temperature of mice tumor injected with PBS showed a slight increase. These data suggested the highly photothermal efficacy of ZHN/ICG NPs, in which temperatures (≥ 50 °C) are sufficient enough to cause irreversible damage to tumors *via* coagulative cell necrosis.⁴⁹ Such successful photoablation of ZHN/ICG NPs eradicated tumor tissues, leaving a dark burned scar at their original sites. Then, the scars healed within 21 days (Fig. 5d and e). In contrast, the tumors treated with free ICG first shrunk but recurred at the 18-day post-injection, while the tumors in the control group showed an increase after laser irradiation as well. These results assured their high potency of ZHN/ICG NPs as photothermal agents. Moreover, the body weights of mice in different groups were not affected significantly (Fig. 5f), demonstrating the biosafety of treatment. Collectively, the ZHN/ICG NPs have successfully demonstrated their photothermal efficiency and biocompatibility in the fluorescence-imaging guided PTT application.

Conclusions

In summary, we have reported a kind of fluorescence imaging-guided photothermal nanotheranostics, which are co-assembled

by the histidine derivative (Z-His-NH₂, ZHN) and clinically used small photoactive indocyanine green (ICG) molecules. Through the combination of multiple noncovalent interactions, the ZHN/ICG nanoparticles (NPs) with high entrapment efficiency were successfully fabricated, which not only maintained the fluorescence properties of ICG molecules, but also enhanced stability against photodegradation and physiological challenges. Under the diagnostic capabilities provided by fluorescence imaging, these ZHN/ICG NPs effectively ablate tumor tissues without recurrence. Compared to the existing nanotheranostics, these nanoparticles offer significant advantages toward anti-tumor clinical translation. On the one hand, the building blocks of both amino acid derivatives and ICG are unparalleled biocompatible and biosafe. On the other hand, the performance of as-prepared nanodrugs, including entrapment efficiency and stability, can be flexibly regulated by the co-assembly strategy. Therefore, the nanodrugs represented in this study hold promise for advancing anti-tumor treatment applications.

Author contributions

Shukun Li, Yudong Li and Mengqian Shi performed the experiments and data analysis; Shukun Li, Ruirui Xing, and Xuehai Yan finished the original manuscript writing and revision; Jan C. M. van Hest critically read the manuscript. All authors discussed the results and implications.

Data availability

The data supporting this article have been included as part of the ESI.†

Conflicts of interest

The authors declare no conflicts of interest.

Acknowledgements

This work was financially supported by the National Science Fund for Distinguished Young Scholars of China (Project No. 22025207), the National Natural Science Foundation of China (Project No. 22207109, 22072154 and 22077122) and the MSCA Postdoctoral Fellowships 2022 (Project No. 101104725). Scheme 1 was created with BioRender.com.

References

- 1 L. Zhao, Y. Liu, R. Xing and X. Yan, *Angew. Chem., Int. Ed.*, 2020, **59**, 3793–3801.
- 2 Y. Wang, R. Garg, D. Cohen-Karni and T. Cohen-Karni, *Nat. Rev. Bioeng.*, 2023, **1**, 193–207.
- 3 J. Yi, L. Y. Liu, W. Gao, J. Zeng, Y. Chen, E. Pang, M. Lan and C. Yu, *J. Mater. Chem. B*, 2024, **12**, 6285–6304.
- 4 C. Y. Tsang and Y. Zhang, *Chem. Soc. Rev.*, 2024, **53**, 2898–2931.



- 5 Y. Li, J. Cui, C. Li, C. Deng, G. Deng, H. Zhang and F. An, *Chin. Chem. Lett.*, 2023, **34**, 108180.
- 6 S. Li, Q. Zou, R. Xing, T. Govindaraju, R. Fakhrullin and X. Yan, *Theranostics*, 2019, **9**, 3249–3261.
- 7 Z. Zhang, Y. Du, X. Shi, K. Wang, Q. Qu, Q. Liang, X. Ma, K. He, C. Chi, J. Tang, B. Liu, J. Ji, J. Wang, J. Dong, Z. Hu and J. Tian, *Nat. Rev. Clin. Oncol.*, 2024, **21**, 449–467.
- 8 P. Cheng and K. Pu, *Nat. Rev. Mater.*, 2021, **6**, 1095–1113.
- 9 P. Cen, J. Huang, C. Jin, J. Wang, Y. Wei, H. Zhang and M. Tian, *Aggregate*, 2023, **4**, e352.
- 10 H. Chen, W. Zhang, G. Zhu, J. Xie and X. Chen, *Nat. Rev. Mater.*, 2017, **2**, 17024.
- 11 R. Chang, L. Zhao, R. Xing, J. Li and X. Yan, *Chem. Soc. Rev.*, 2023, **52**, 2688–2712.
- 12 R. Chang, Q. Zou, L. Zhao, Y. Liu, R. Xing and X. Yan, *Adv. Mater.*, 2022, **34**, 2200139.
- 13 X. Mu, F. Wu, Y. Tang, R. Wang, Y. Li, K. Li, C. Li, Y. Lu, X. Zhou and Z. Li, *Aggregate*, 2022, **3**, e170.
- 14 P. Zhu, S. Wang, Y. Zhang, Y. Li, Y. Liu, W. Li, Y. Wang, X. Yan and D. Luo, *ACS Appl. Bio Mater.*, 2022, **5**, 2031–2045.
- 15 P. K. Jain, X. Huang, I. H. El-Sayed and M. A. El-Sayed, *Acc. Chem. Res.*, 2008, **41**, 1578–1586.
- 16 X. Wang, X. Zhong, J. Li, Z. Liu and L. Cheng, *Chem. Soc. Rev.*, 2021, **50**, 8669–8742.
- 17 J. Hu, D. Wu, Q. Pan, H. Li, J. Zhang and F. Geng, *ACS Appl. Nano Mater.*, 2022, **5**, 14171–14190.
- 18 S. K. Hari, A. Gauba, N. Shrivastava, R. M. Tripathi, S. K. Jain and A. K. Pandey, *Drug Delivery Transl. Res.*, 2023, **13**, 135–163.
- 19 Y. Zhang, C. Y. Ang and Y. Zhao, *Polym. J.*, 2016, **48**, 589–603.
- 20 J. Scheerstra, A. Wauters, J. Tel, L. Abdelmohsen and J. van Hest, *Mater. Today Adv.*, 2022, **13**, 100203.
- 21 N. Aibani, T. N. Khan and B. Callan, *Int. J. Pharm. X*, 2020, **2**, 100040.
- 22 I. Fox and E. Wood, *Proc. Staff Meet. Mayo Clin.*, 1960, **35**, 732–744.
- 23 W. Zhang, S. Li, Y. Liu, R. Xing, Z. Jin, X. Yan and H. Xue, *Nano Today*, 2023, **50**, 101832.
- 24 H. Wang, X. Li, B. Tse, H. Yang, C. Thorling, Y. Liu, M. Touraud, J. Chouane, X. Liu, M. Roberts and X. Liang, *Theranostics*, 2018, **8**, 1227–1242.
- 25 H. Yang, H. Liu, W. Hou, J. Gao, Y. Duan, D. Wei, X. Gong, H. Wang, X. Wu and J. Chang, *J. Mater. Chem. B*, 2020, **8**, 251–259.
- 26 F. An, Z. Yang, M. Zheng, T. Mei, G. Deng, P. Guo, Y. Li and R. Sheng, *J. Nanobiotechnol.*, 2020, **18**, 49.
- 27 W. Shan, R. Chen, Q. Zhang, J. Zhao, B. Chen, X. Zhou, S. Ye, S. Bi, L. Nie and L. Ren, *Adv. Mater.*, 2018, **30**, 1707567.
- 28 S. Li, R. Xing, J. van Hest and X. Yan, *Expert Opin. Drug Delivery*, 2022, **19**, 847–860.
- 29 S. Li, R. Chang, L. Zhao, R. Xing, J. van Hest and X. Yan, *Nat. Commun.*, 2023, **14**, 5227.
- 30 C. Yuan, R. Xing, J. Cui, W. Fan, J. Li and X. Yan, *CCS Chem.*, 2024, **6**, 255–265.
- 31 Y. Pan, M. Suo, Q. Huang, M. Lyu, Y. Jiang, S. Wang, W. Tang, S. Ning and T. Zhang, *Aggregate*, 2024, **5**, e432.
- 32 X. Hu, M. Liao, H. Gong, L. Zhang, H. Cox, T. Waigh and J. Lu, *Curr. Opin. Colloid Inter. Sci.*, 2020, **45**, 1–13.
- 33 R. Xing, C. Yuan, W. Fan, X. Ren and X. Yan, *Sci. Adv.*, 2023, **9**, eadd8105.
- 34 R. Chang, C. Yuan, P. Zhou, R. Xing and X. Yan, *Acc. Chem. Res.*, 2024, **57**, 289–301.
- 35 S. Li, W. Zhang, R. Xing, C. Yuan, H. Xue and X. Yan, *Adv. Mater.*, 2021, **33**, 2100595.
- 36 R. Xing, Q. Zou, C. Yuan, L. Zhao, R. Chang and X. Yan, *Adv. Mater.*, 2019, **31**, 1900822.
- 37 S. Li, Y. Tan, L. Zhang and C. Zhou, *Pharmaceutics*, 2023, **15**, 1348.
- 38 G. Chen, I. Roy, C. Yang and P. N. Prasad, *Chem. Rev.*, 2016, **116**, 2826–2885.
- 39 Y. Huang, J. Xing, Q. Gong, L. Chen, G. Liu, C. Yao, Z. Wang, H. Zhang, Z. Chen and Q. Zhang, *Nat. Commun.*, 2019, **10**, 169.
- 40 Y. Ding, C. Wang, B. Lu and Y. Yao, *Front. Chem.*, 2021, **9**, 775436.
- 41 D. Roper, W. Ahn and M. Hoepfner, *J. Phys. Chem. C*, 2007, **111**, 3636–3641.
- 42 K. Nienhaus, H. Wang and G. U. Nienhaus, *Mater. Today Adv.*, 2020, **5**, 100036.
- 43 A. Tukova, Y. Nie, M. Tavakkoli Yarak, N. T. Tran, J. Wang, A. Rodger, Y. Gu and Y. Wang, *Aggregate*, 2023, **4**, e323.
- 44 S. Li, Q. Zou, Y. Li, C. Yuan, R. Xing and X. Yan, *J. Am. Chem. Soc.*, 2018, **140**, 10794–10802.
- 45 T. Sun, J. Guo, H. Wen, Q. Pei, Q. Wu, D. Hao, C. Dou and Z. Xie, *Aggregate*, 2023, **4**, e362.
- 46 M. Liang, L. Liu, Y. Sun, J. Li, L. E. Zhang, X. Jiang and W. Wu, *Aggregate*, 2024, **5**, e458.
- 47 A. Marabelle, H. Kohrt, C. Caux and R. Levy, *Clin. Cancer Res.*, 2014, **20**, 1747–1756.
- 48 C. Lim, E. Vibert, D. Azoulay, C. Salloum, T. Ishizawa, R. Yoshioka, Y. Mise, Y. Sakamoto, T. Aoki and Y. Sugawara, *J. Visc. Surg.*, 2014, **151**, 117–124.
- 49 G. Hannon, F. Tansi, I. Hilger and A. Prina-Mello, *Adv. Ther.*, 2021, **4**, 2000267.

